



TESS-Keck Survey. IX. Masses of Three Sub-Neptunes Orbiting HD 191939 and the Discovery of a Warm Jovian plus a Distant Substellar Companion

Jack Lubin¹ , Judah Van Zandt² , Rae Holcomb¹ , Lauren M. Weiss³ , Erik A. Petigura² , Paul Robertson¹ , Joseph M. Akana Murphy^{4,23} , Nicholas Scarsdale⁴ , Konstantin Batygin⁵ , Alex S. Polanski⁶ , Natalie M. Batalha⁴ , Ian J. M. Crossfield⁶, Courtney Dressing⁷ , Benjamin Fulton⁸ , Andrew W. Howard⁹ , Daniel Huber³ , Howard Isaacson^{7,10} , Stephen R. Kane¹¹ , Arpita Roy^{12,13} , Corey Beard¹ , Sarah Blunt^{9,23} , Ashley Chontos^{3,23} , Fei Dai¹⁴ , Paul A. Dalba^{11,24} , Kaz Gary⁶, Steven Giacalone⁷ , Michelle L. Hill¹¹ , Andrew Mayo⁷ , Teo Močnik¹⁵ , Molly R. Kosiarek^{16,23} , Malena Rice^{17,23} , Ryan A. Rubenzahl^{9,23} , David W. Latham¹⁸ , S. Seager^{19,20,21} , Joshua N. Winn²² , and Kaz Gary⁶

¹ Department of Physics & Astronomy, University of California, Irvine, Irvine, CA 92697, USA

² Department of Physics & Astronomy, University of California, Los Angeles, Los Angeles, CA 90095, USA

³ Institute for Astronomy, University of Hawai'i, 2680 Woodlawn Drive, Honolulu, HI 96822, USA

⁴ Department of Astronomy and Astrophysics, University of California, Santa Cruz, CA 95060, USA

⁵ Division of Geological and Planetary Sciences, California Institute of Technology, Pasadena, CA 91125, USA

⁶ Department of Physics & Astronomy, University of Kansas, 1082 Malott, 1251 Wescoe Hall Drive, Lawrence, KS 66045, USA

⁷ Department of Astronomy, University of California Berkeley, Berkeley CA 94720, USA

⁸ NASA Exoplanet Science Institute/Caltech-IPAC, MC 314-6, 1200 E. California Boulevard, Pasadena, CA 91125, USA

⁹ Department of Astronomy, California Institute of Technology, Pasadena, CA 91125, USA

¹⁰ Centre for Astrophysics, University of Southern Queensland, Toowoomba, QLD, Australia

¹¹ Department of Earth and Planetary Sciences, University of California, Riverside, Riverside, CA 92521, USA

¹² Space Telescope Science Institute, 3700 San Martin Drive, Baltimore, MD 21218, USA

¹³ Department of Physics and Astronomy, Johns Hopkins University, 3400 N. Charles Street, Baltimore, MD 21218, USA

¹⁴ Division of Geological and Planetary Sciences, 1200 E. California Boulevard, Pasadena, CA 91125, USA

¹⁵ Gemini Observatory/NSF's NOIRLab, 670 N. A'ohoku Place, Hilo, HI 96720, USA

¹⁶ Department of Astronomy and Astrophysics, University of California, Santa Cruz, Santa Cruz, CA 95064, USA

¹⁷ Department of Astronomy, Yale University, New Haven, CT 06511, USA

¹⁸ Center for Astrophysics | Harvard & Smithsonian, 60 Garden Street, Cambridge, MA 02138, USA

¹⁹ Department of Physics and Kavli Institute for Astrophysics and Space Research, Massachusetts Institute of Technology, Cambridge, MA 02139, USA

²⁰ Department of Earth, Atmospheric and Planetary Sciences, Massachusetts Institute of Technology, Cambridge, MA 02139, USA

²¹ Department of Aeronautics and Astronautics, MIT, 77 Massachusetts Avenue, Cambridge, MA 02139, USA

²² Department of Astrophysical Sciences, Princeton University, 4 Ivy Lane, Princeton, NJ 08544, USA

Received 2021 April 21; revised 2021 November 17; accepted 2021 November 24; published 2022 January 31

Abstract

Exoplanet systems with multiple transiting planets are natural laboratories for testing planetary astrophysics. One such system is HD 191939 (TOI 1339), a bright ($V=9$) and Sun-like (G9V) star, which TESS found to host three transiting planets (b, c, and d). The planets have periods of 9, 29, and 38 days each with similar sizes from 3 to $3.4 R_{\oplus}$. To further characterize the system, we measured the radial velocity (RV) of HD 191939 over 415 days with Keck/HIRES and APF/Levy. We find that $M_b = 10.4 \pm 0.9 M_{\oplus}$ and $M_c = 7.2 \pm 1.4 M_{\oplus}$, which are low compared to most known planets of comparable radii. The RVs yield only an upper limit on M_d ($< 5.8 M_{\oplus}$ at 2σ). The RVs further reveal a fourth planet (e) with a minimum mass of $0.34 \pm 0.01 M_{\text{Jup}}$ and an orbital period of 101.4 ± 0.4 days. Despite its nontransiting geometry, secular interactions between planet e and the inner transiting planets indicate that planet e is coplanar with the transiting planets ($\Delta i < 10^\circ$). We identify a second high-mass planet (f) with 95% confidence intervals on mass between 2 and $11 M_{\text{Jup}}$ and period between 1700 and 7200 days, based on a joint analysis of RVs and astrometry from Gaia and Hipparcos. As a bright star hosting multiple planets with well-measured masses, HD 191939 presents many options for comparative planetary astronomy, including characterization with JWST.

Unified Astronomy Thesaurus concepts: [Exoplanet astronomy \(486\)](#); [Exoplanet dynamics \(490\)](#)

Supporting material: machine-readable table

1. Introduction

Bright systems with multiple planets are valuable to the exoplanet community. They are amenable to precise radial velocity (RV) monitoring and are natural laboratories of planetary astrophysics. With multiple planets forming from the same protoplanetary disk, such systems allow for comparative exoplanetology investigations, as we can assume a similar history of formation conditions for each planet.

NASA's Transiting Exoplanet Survey Satellite (TESS; Ricker et al. 2015) is an all-sky photometric survey searching for planets

²³ NSF Graduate Research Fellow.

²⁴ NSF Astronomy and Astrophysics Postdoctoral Fellow.



around the brightest stars, and its discoveries continue to deliver new planetary systems for detailed investigation. Due to the 28-day per sector survey strategy, TESS is finding many exoplanets in short-period orbits (<14 days). A primary science goal of the TESS mission is to measure the masses of 50 planets smaller than 4 Earth radii.

The TESS-Keck Survey (TKS) is a collaboration among astronomers at Keck partner institutions to combine efforts and telescope time to meet and exceed this science goal (see TKS-0 (Chontos et al. 2021), TKS-I (Dalba et al. 2020), TKS-II (Weiss et al. 2021), TKS-III (Dai et al. 2020), TKS-IV (Rubenzahl et al. 2021)). Our survey is further concerned with the formation, evolution, and dynamics of various types of exoplanetary systems. Three of TKS’s main goals are characterizing systems with multiple planets, those with possible distant giant planets, and those that show promise for high-quality atmospheric characterization (Chontos et al. 2021)

HD 191939 is a solar-like star (G9V) that hosts a multiplanet system that addresses most of our areas of interest. TESS observed the star for 252 days in 9 nonconsecutive sectors during its primary mission, allowing for a long baseline (326 days) of photometry and enabling discovery of longer-period planets. Badenas-Agusti et al. (2020) have already announced three transiting planets, two of which would not have been discovered without multiple sectors of coverage. This work includes the first mass measurements of the transiting planets, and we have uncovered an additional Jovian planet as well as a high-mass planet. In all, this system has a wide diversity of planet masses and periods.

We find that the transiting planets of HD 191939 fall into some of the patterns uncovered by statistics papers on the Kepler planets. They have nearly identical radii, as is typical of the Kepler planets (Weiss et al. 2018), yet their spacing is irregular. They have similar masses, consistent with the pattern found in Millholland et al. (2017), but the planets have low masses for their sizes (Weiss & Marcy 2014), implying lower-than-average densities. The masses we present are some of the most precise mass measurements of small transiting planets in a multiplanet system (two of three with 5σ mass or better).

In this paper, we describe our data sources (Section 2) and analyze the system properties, describing the host star properties (Section 3.1) and our RV model (Section 3.2) and photometry model (Section 3.3). Next, we describe the densities and compositions of the transiting planets (Section 4). We then explore the system dynamics in detail, including constraining the properties of planet f with new techniques (Section 5), placing limits on the inclination of planet e (Section 6), and describing the resonant interactions of planets c and d (Section 7). We then quantify the possibility of additional planets in the system (Section 8) before investigating follow-up opportunities for HD 191939 by examining the system’s atmospheric and Rossiter–McLaughlin prospects (Section 9). We present our conclusions in Section 10.

2. Observations

2.1. TESS Photometry

Due to the star’s high northern decl., TESS observed HD 191939 for a total of nine sectors in Cycle 2. Data were obtained with a 2-minute cadence during sectors 15–19, 21–22, and 24–25, spanning a total baseline of 326 days from 2019 July 18 to 2020 June 8, though the star was not observed for the

entirety of this time (Stassun et al. 2018). We downloaded data processed through the Science Processing Operations Center (SPOC) pipeline through the Mikulski Archive for Space Telescopes (MAST) and used the Pre-search Data Conditioning (PDC) light curves for our analysis (Jenkins et al. 2016).

2.2. Radial Velocities

We acquired 73 RV observations with Keck/HIRES at the W. M. Keck Observatory on Maunakea, Hawaii, between 2019 November and 2020 December; see Table 2. We reduced the spectra in the standard procedure of the California Planet Search (Howard et al. 2010). We used a high signal-to-noise ratio (S/N) template from Keck/HIRES to generate a deconvolved stellar spectral template (DSST). We took all RV observations with a warm iodine cell in the light path for wavelength calibration (Valenti et al. 1995; Butler et al. 1996), with a median S/N of $\sim 216 \text{ pixel}^{-1}$ at the iodine wavelength region of $\sim 500 \text{ nm}$.

We also acquired 104 RV observations with the Automated Planet Finder telescope (APF; Vogt et al. 2014) at Lick Observatory in California between 2019 December and 2020 December. At the beginning of the baseline, we observed twice per night and binned the two observations. After 2020 February, we changed our observing strategy to obtain one spectrum per night owing to time constraints within our survey. We used the same Keck/HIRES template to calculate the APF RVs because it produced a higher-quality DSST than the APF template. The median S/N for APF observations was $\sim 76 \text{ pixel}^{-1}$ at the iodine wavelength region of $\sim 500 \text{ nm}$. To maintain only high-quality data points, we removed all (seven) RVs from the APF time series that had $S/N < 31$, equivalent to an RV error of 9 m s^{-1} . We also removed one APF observation that was taken within 5 minutes of 12° twilight in the morning.

3. System Properties

3.1. Host Star

We analyzed our iodine-free HIRES spectrum with the *SpecMatch-Syn* code (Petigura et al. 2017) to derive the T_{eff} , $\log g$, and metallicity [Fe/H] of the host star, and we list our results in Table 1. We then derived stellar mass, radius, and age according to the approach described in Fulton & Petigura (2018). We incorporated Gaia DR2 parallaxes (Gaia Collaboration et al. 2018), Two Micron All Sky Survey apparent K magnitude, and the MIST models (Choi et al. 2016) using the *isoclassify* package (Huber et al. 2017; Berger et al. 2020). Following Tayar et al. (2020), we inflated the error bar on the stellar mass measurement by adding a systematic error term of $0.03 M_\odot$ in quadrature. Given the limited spread in the H-R diagram at HD 191939’s T_{eff} ($5348 \pm 100 \text{ K}$, G9V), isochrone ages have large uncertainties. However, they indicate that this star is older than 8.7 Gyr (2σ confidence).

We determined the abundances for 15 individual elements using *KeckSpec* (Rice & Brewer 2020), finding that the composition of HD 191939 is generally subsolar for most elements. We determine the Mg/Si ratio to be consistent with both the solar value and most local stars (Brewer & Fischer 2017). C/O, however, is found to be 0.34 ± 0.09 , 2σ lower than the solar value, implying that the assumption of solar abundances for these elements may not be applicable to stellar atmospheric models. We obtain $[Y/Mg] = -0.08 \pm 0.1$ and use this with the abundance–age relation of Nissen et al. (2020),

Table 1
System Parameters

Stellar Parameters					
Parameter	Value	Source			
General					
Other names	TOI 1339, HIP 99175				
R.A.	20:08:06.15	Gaia Collaboration et al. (2018)			
decl.	+66:51:01.08	Gaia Collaboration et al. (2018)			
V mag	8.97	Badenas-Agusti et al. (2020)			
Astrometry					
Parallax (mas)	18.71 ± 0.07	Badenas-Agusti et al. (2020)			
Proper motion in R.A. (mas)	150.26 ± 0.04	Badenas-Agusti et al. (2020)			
Proper motion in decl. (mas)	-63.91 ± 0.05	Badenas-Agusti et al. (2020)			
Radial velocity (km s^{-1})	-9.5 ± 0.2	Gaia Collaboration et al. (2018)			
SpecMatch Spectroscopy					
T_{eff} (K)	5348 ± 100	SpecMatch-Synthetic			
$\log g$ (cm s^{-2})	4.3 ± 0.1	SpecMatch-Synthetic			
[Fe/H] (dex)	-0.15 ± 0.06	SpecMatch-Synthetic			
$v \sin i$ (km s^{-1})	<2.0	SpecMatch-Synthetic			
$\log R'_{\text{HK}}$ (dex)	-5.11 ± 0.05	SpecMatch-Synthetic			
Spectral type	G9V	Pecaut & Mamajek (2013)			
Isochrone Modeling					
Radius, R_* (R_{\odot})	0.94 ± 0.02	Isoclassify			
Mass, M_* (M_{\odot})	0.81 ± 0.04	Isoclassify Before following Tayar et al. (2020), error was ± 0.03			
Luminosity, L_* (L_{\odot})	0.65 ± 0.02	Isoclassify			
Age (Gyr)	>8.7	Isoclassify			
Stellar Abundances (Dex) from KeckSpec					
[C/H]	-0.12 ± 0.07	[N/H]	-0.17 ± 0.09		
[O/H]	0.09 ± 0.09	[Na/H]	-0.18 ± 0.07		
[Mg/H]	-0.09 ± 0.04	[Al/H]	-0.02 ± 0.08		
[Si/H]	-0.11 ± 0.06	[Ca/H]	-0.17 ± 0.07		
[Ti/H]	-0.07 ± 0.05	[V/H]	-0.12 ± 0.07		
[Cr/H]	-0.26 ± 0.05	[Mn/H]	-0.38 ± 0.07		
[Ni/H]	-0.21 ± 0.05	[Y/H]	-0.17 ± 0.09		
Planet Parameters					
Parameter	Planet b	Planet c	Planet d	Planet e	Planet f
Orbital period (days)	8.88029 ± 0.00002	28.5805 ± 0.0002	38.3525 ± 0.0003	101.5 ± 0.4	1700–7200
Time of conjunction (BJD)	$2,458,715.3561 \pm 0.0004$	$2,458,726.0534 \pm 0.0006$	$2,458,743.5518 \pm 0.0007$	$2,459,043.6 \pm 0.3$...
Duration (hours)	3.1 ± 0.1	4.5 ± 0.2	5.5 ± 0.3
Impact parameter	0.62 ± 0.02	0.63 ± 0.02	0.48 ± 0.04
Inclination (deg)	88.06 ± 0.08	89.09 ± 0.03	89.43 ± 0.04	$88.0\text{--}89.4$...
R_p/R_*	0.0336 ± 0.0007	0.0306 ± 0.0007	0.0302 ± 0.0007
Radius (R_{\oplus})	3.39 ± 0.07	3.08 ± 0.07	3.04 ± 0.07
Semimajor axis (au)	0.078 ± 0.001	0.170 ± 0.002	0.207 ± 0.003	0.397 ± 0.005	$2.6\text{--}7.0$
^a Equilibrium temperature (K)	893 ± 36	605 ± 24	549 ± 22	397 ± 16	...
Eccentricity	0 (fixed)	0 (fixed)	0 (fixed)	0 (fixed)	0 (fixed)

Table 1
(Continued)

Stellar Parameters					
Parameter	Value	Source			
RV semiamplitude (ms^{-1})	3.8 ± 0.3	1.8 ± 0.3	0.6 ± 0.3	17.2 ± 0.4	>23.0
Mass (M_{\oplus})	10.4 ± 0.9	7.2 ± 1.4	<5.8 at 2σ	$108 \pm 3/\sin i$	630-3500
Density (g cm^{-3})	1.5 ± 0.2	1.4 ± 0.3	0.5 ± 0.3
Model Parameters					
Parameter	Value				
Linear limb coefficient, u_1	0.42 ± 0.06				
Quadratic limb coefficient, u_2	0.05 ± 0.08				
HIRES zero-point, γ_{HIRES} (ms^{-1})	-22.26				
HIRES jitter, σ_{HIRES} (ms^{-1})	1.7 ± 0.2				
APF zero-point, γ_{APF} (ms^{-1})	-8.01				
APF jitter, σ_{APF} (ms^{-1})	3.7 ± 0.6				
Trend, $\dot{\gamma}$ ($\text{ms}^{-1} \text{ day}^{-1}$)	0.114 ± 0.006				
Curve, $\ddot{\gamma}$ ($\text{ms}^{-1} \text{ day}^{-2}$)	$(-6 \pm 2) \times 10^{-5}$				

Note.

^a Equilibrium temperatures assume zero bond albedo.

which gives an age estimate of 7 ± 3 Gyr. Although this is consistent with the lower bound obtained from an isochronal fit, HD 191939 is 400 K cooler than the Sun-like stars used for this relation and should be treated with caution.

HD 191939 is a chromospherically inactive star with $\log R'_{\text{HK}} = -5.11 \pm 0.05$. We computed the Ca II H and K index (S_{HK}) as described in Isaacson & Fischer (2010) for both our Keck/HIRES and APF time series; see Table 2. We find no significant correlations between the S_{HK} values and RVs. Additionally, we find no statistically significant periodicities in the S_{HK} time series.

3.2. RV Model

Soon after beginning our RV observations, we saw evidence of an additional planet beyond those identified by TESS, including observations that showed a $\sim 40 \text{ m s}^{-1}$ change in the RV, consistent with a massive planet. Continued observations further traced a large-amplitude periodicity near ~ 100 days. The Generalized Lomb–Scargle (GLS) periodogram (Zechmeister & Kürster 2009) of the RVs is dominated by this signal, which we attribute to a fourth planet (e) (Figure 1, top panel).

To discern the architecture of the system, we performed a model comparison analysis. Using RadVel (Fulton et al. 2018), we tested a variety of RV models: three to five total planets, and either allowing eccentricity to vary for each or fixing it to zero, as well as allowing or prohibiting trend and/or curvature terms. We used Markov Chain Monte Carlo (MCMC) to explore the parameter space and estimate uncertainties; all planet models discussed here converged by the default RadVel criteria unless otherwise stated.

In all models, we fixed the periods and times of conjunction of the transiting planets to the values found from our TESS photometry model. We set uniform priors on the Doppler

Table 2
RADIAL VELOCITY TIME SERIES

BJD	RV (m s^{-1})	RV err (m s^{-1})	S-Value	S-Value err	Instrument
2,458,795.832	-20.961	1.225	0.146	0.001	HIRES
2,458,802.800	-9.760	1.291	0.146	0.001	HIRES
2,458,815.779	-14.967	1.241	0.142	0.001	HIRES
2,458,834.647	1.901	3.891	0.141	0.002	APF
2,458,834.661	8.670	3.813	0.145	0.002	APF
2,458,837.734	-6.977	4.347	0.176	0.002	APF

(This table is available in its entirety in machine-readable form.)

amplitudes $(-\infty, \infty)$, allowing negative values for all planets to avoid biasing the masses to higher values. We set a uniform prior from 1 to 1000 days on the period of planet e and a uniform prior on its time of conjunction (2,459,000, 2,459,100) BJD. For both instruments, we set a prior on the instrumental jitter as uniform (0, 10) m s^{-1} . Lastly, we set a prior on the trend term uniform from $(-1, 1) \text{ m/s/d}$ and on the curvature term uniform $(-0.1, 0.1) \text{ m/s/d}^2$.

Our preferred RV model has an Akaike Information Criterion (AIC; Akaike 1974) of 858 and contains four planets on circular orbits, as well as both a trend and a curvature term, which models a subset of a sinusoid as a quadratic to represent a fifth body in the system. The closest neighboring model, in terms of AIC, is one with four planets plus a trend but no curvature term (AIC = 866). Our preferred model is very strongly preferred over a model with three transiting planets (did not converge, AIC = 1332) and a four-planet model with

Table 3
TRANSIT MDTIMES

Planet	Epoch #	Midtime (BJD)	Error (BJD)
b	1	2,458,715.3552	0.0023
b	3	2,458,733.1156	0.0028
b	4	2,458,741.9962	0.0023
b	6	2,458,759.7587	0.0024
b	7	2,458,768.6376	0.0029
b	9	2,458,786.3987	0.0021
b	10	2,458,795.2825	0.0026
b	11	2,458,804.1602	0.0026
b	12	2,458,813.0424	0.0041
b	13	2,458,821.9181	0.0023
b	14	2,458,830.8014	0.0029
b	15	2,458,839.6806	0.0018
b	19	2,458,875.2017	0.0018
b	21	2,458,892.9626	0.0020
b	22	2,458,901.8430	0.0020
b	23	2,458,910.7222	0.0023
b	24	2,458,919.6017	0.0024
b	29	2,458,964.0028	0.0036
b	30	2,458,972.8837	0.0021
b	31	2,458,981.7649	0.0021
b	32	2,458,990.6450	0.0020
b	33	2,458,999.5248	0.0029
b	34	2,459,008.4056	0.0023
<hr/>			
c	1	2,458,726.0546	0.0033
c	2	2,458,754.6340	0.0028
c	3	2,458,783.2116	0.0031
c	4	2,458,811.7992	0.0031
c	5	2,458,840.3758	0.0029
c	7	2,458,897.5359	0.0038
c	8	2,458,926.1168	0.0031
<hr/>			
d	1	2,458,743.5531	0.0038
d	2	2,458,781.9029	0.0029
d	3	2,458,820.2645	0.0031
d	5	2,458,896.9613	0.0038
d	6	2,458,973.6648	0.0031

no trend and no curvature (AIC = 1202). Our full RV time series can be seen in Figure 2, and phase-folded RV time series for each planet can be seen in Figure 3. The orbital parameters and masses of all planets can be found in Table 1. Our full RV time series in a machine-readable format is available in Table 3. We searched the residuals of our preferred model for additional planets but found no statistically significant signals.

3.3. Photometry Model

We pre-whitened the TESS photometry by using a Gaussian process model to subtract out low-amplitude stellar and instrumental variability from the light curve. We then performed a blind transit search using Transit Least Squares (TLS; Hippke & Heller 2019). This recovered three transiting planets with period, depth, and duration values and errors consistent with the previously published values in Badenas-Agusti et al. (2020). We also performed a more targeted search with TLS for transits of planet e but found no evidence of any such events. We then modeled the transits of planets b, c, and d with the Exoplanet package (Foreman-Mackey et al. 2020b) and rederived planet parameters using our updated stellar parameters and the TLS output as priors (Table 1).

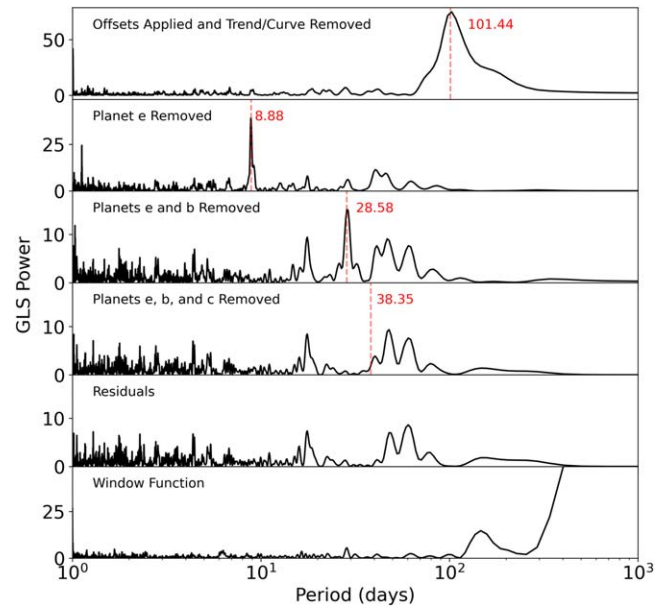


Figure 1. GLS periodograms of the combined time series of Keck/HIRES and APF data. The two data sets were first filtered by removing instrumental offsets and the trend and curvature according to the best-fit parameters from our preferred model. In each descending panel, we have removed one planet at a time. The bottom panel shows the window function of the time series.

To calculate this model, we assumed circular orbits and fit for 17 parameters: (1) orbital periods, with Gaussian priors informed by our TLS search values; (2) times of inferior conjunction, with Gaussian priors informed by our TLS search; (3) planet-to-star radius ratios, with a log-uniform prior from 0.01 to 0.1; (4) impact parameters, with a uniform prior from 0 to 1; (5) stellar radius, with Gaussian priors defined by the updated stellar parameters; (6) stellar mass, with Gaussian priors defined by the updated stellar parameters; (7) quadratic limb-darkening parameters calculated using Python Limb Darkening Toolkit (Parviainen & Aigrain 2015); and (8) a white-noise scaling term for the TESS light curve. Exoplanet implements the MCMC algorithm, which we ran with 2000 iterations and a 500-step burn-in and found that all chains converged. Additionally, we derived transit mid-points for each transit of each planet, which is discussed further in Section 7 (see the Table 2). Figure 4 shows our modeled phase-folded light curves for each planet, and Figure 5 shows the full reduced TESS light curve of the star with transits color-coded.

Given our weak detection of planet d in the RV time series, we returned to the photometry to confirm the period and transit times. Due to the positioning of data gaps in the light curve, there are four “odd” transits and one “even” transit of planet d. We considered the possibility that the single even transit, occurring at 2,458,781.89 BJD, comes from a different source than the four odd transits. In such a scenario, the orbital period of planet d would double to 76.7 days. However, comparing between the transits, including matching depths, durations, and ingress/egress shapes, we found no inconsistencies between the single transit and the other four. Furthermore, we find no evidence for a ~ 76 -day periodicity in our RV time series. Thus, we conclude that all five transits do originate from a single planet with an orbital period of 38.4 days.

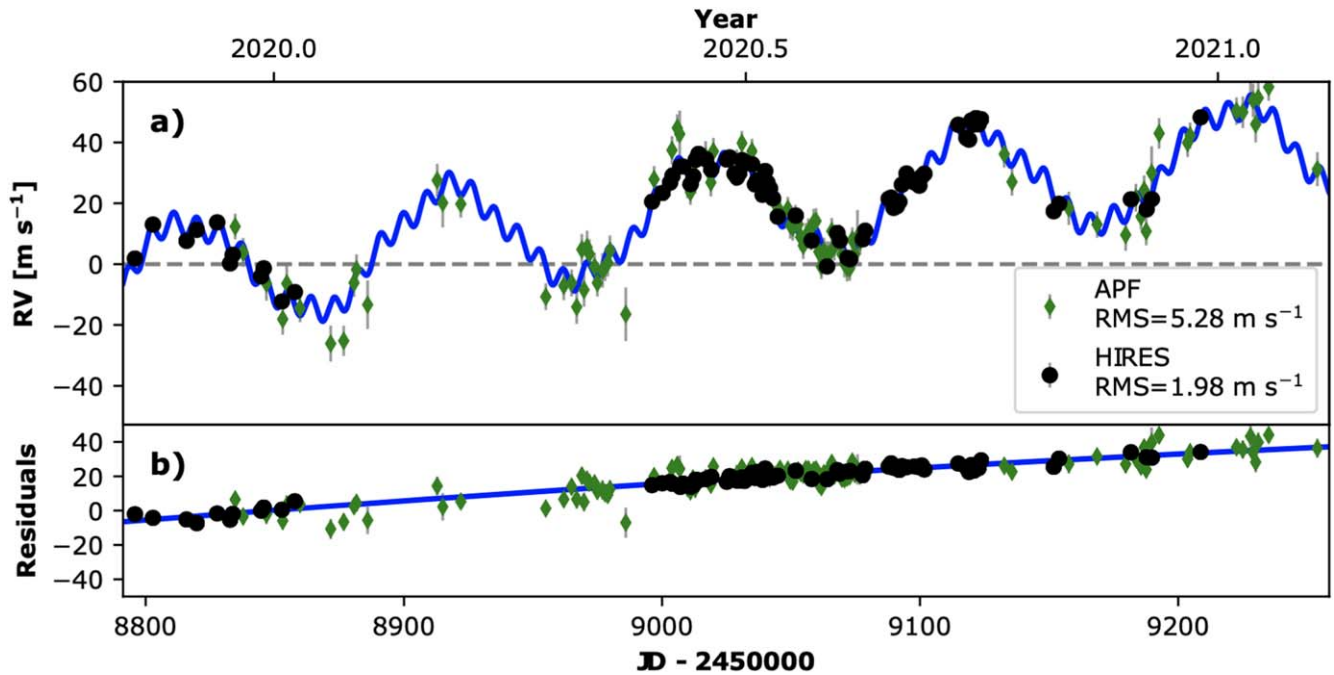


Figure 2. (a) Our complete RV time series with our preferred model (blue); (b) residuals including trend and curvature. Data collected from Keck/HIRES are shown as black circles, while data from the APF are shown by green diamonds.

4. Composition of Transiting Planets

How do the transiting planets in this system compare to other known transiting planets? We find that planet b imparts a Doppler semiamplitude of $3.8 \pm 0.3 \text{ ms}^{-1}$, corresponding to a mass of $10.4 \pm 0.9 M_{\oplus}$; planet c imparts $1.8 \pm 0.3 \text{ ms}^{-1}$, corresponding to $7.2 \pm 1.4 M_{\oplus}$; and planet d imparts $0.6 \pm 0.3 \text{ ms}^{-1}$, corresponding to $2.8 \pm 1.5 M_{\oplus}$. The placement of the three transiting planets on a mass–radius diagram reveals that they exist at the periphery of the known planet population (Figure 6). Planet b fits more consistently with previously known planets, while planet d is a low-mass outlier. The relatively low masses for their radii imply small densities. We find that planet b has a bulk density of $1.5 \pm 0.2 \text{ g cm}^{-3}$, planet c has $1.4 \pm 0.3 \text{ g cm}^{-3}$, and planet d has $0.5 \pm 0.3 \text{ g cm}^{-3}$.

Fulton et al. (2017) and Van Eylen et al. (2018) described the radius gap as a region of radius phase space from 1.5 to $2.0 R_{\oplus}$, where relatively few planets are found. Studies have explained this gap as most likely due to a transitional phase between planets with and without extended H/He envelopes, which may be due to photoevaporation (Lopez & Fortney 2014; Owen & Wu 2017). Given that all three transiting planets in the HD 191939 system have radii above the gap, it is likely that the best description of their compositions is that of a volatile-rich envelope surrounding a rocky core (Weiss & Marcy 2014; Rogers 2015; Fulton et al. 2017). Employing *Smint* (Piaulet et al. 2021), which interpolates the model grids from Lopez & Fortney (2014) and Zeng et al. (2016) and samples posterior space with MCMC, we explored the possible fractions of H/He by mass for the three transiting planets assuming a dry, Earth-like, rock-iron core. Using a flat prior for the age from 9 to 13 Gyr, we find H/He envelopes of $6.5\% \pm 0.5\%$ for planet b, $5.7\% \pm 0.6\%$ for planet c, and $6.4\% \pm 0.5\%$ for planet d.

From our RV model, we place a 2σ upper limit on planet d’s mass at $5.8 M_{\oplus}$. This corresponds to a 2σ upper limit on planet d’s density of 1.1 g cm^{-3} . While this density upper limit places it within the range of planets b and c, the potential low density

for planet d is noteworthy. In the literature, there is a population of low-density planets: the Kepler-51 system (Masuda 2014), Kepler-79d (Jontof-Hutter et al. 2014), and Kepler-87 c (Ofir et al. 2014), which are collectively described as “super-puffs” for their inflated radii ($4\text{--}8 R_{\oplus}$) and low masses ($2\text{--}5 M_{\oplus}$), which imply densities of $\sim 0.1 \text{ g cm}^{-3}$. While HD 191939 d is not a super-puff since its radius is smaller (only $3 R_{\oplus}$), it does share a notable characteristic with the super-puffs: they all exist in or near resonance with another planet in their systems. The super-puff planets may have low masses for their sizes as part of a selection bias: the planet masses are derived from transit timing variation (TTV) interactions, which are most prominent for planets in or near a resonance chain. HD 191939 d’s potential low density, combined with its placement as the outer member of a near 4:3 resonance with planet c (see Section 7 for more detail), draws some comparison to the super-puffs and brings forward questions on its possible formation history.

Two different mechanisms have been proposed for explaining the prevalence of highly inflated planets in or near resonance. Lee & Chiang (2016) showed that super-puff planets most easily gain their extended atmospheres in dust-free environments at distances beyond 1 au before migrating inward. As part of this migration, they are more likely to form the outer companion of a resonance chain with another interior planet in the system. Under this formation scenario, planet d would likely contain a large fraction of water, a composition that we do not explore in this paper. Millholland (2019) describes how super-puffs that exist just wide of resonance with another planet are thought to have preferentially high obliquities, which could drive heat dissipation through obliquity tides, resulting in inflated planet radii.

HD 191939 d represents a unique opportunity to study a possible low-density planet and to test the above theories for two reasons. The mass measurement we provide comes from the RV method rather than TTVs. The location in the system interior to the Jovian planet e can provide dynamical

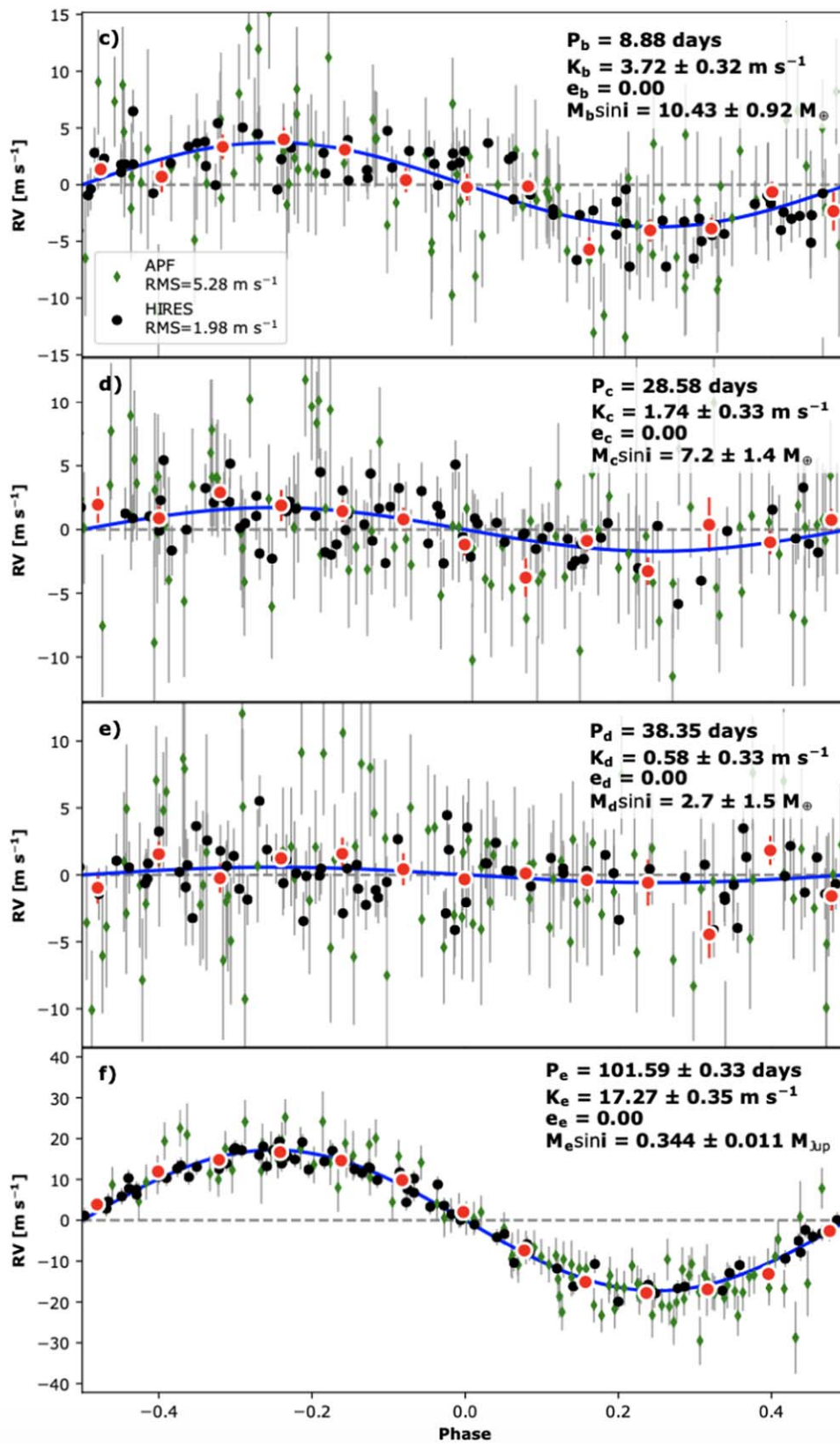


Figure 3. The phase-folded RV time series for each planet with periods less than our baseline. Red circles are bins of size 0.08 phase.

constraints for any potential migration history. Of the super-puffs listed above, only Kepler-79d has a confirmed planet exterior to its orbit in the system, and this planet is another sub-Neptune.

The relatively small masses, low densities, and high equilibrium temperatures of these planets might combine to drive atmospheric escape on some or all of the three inner planets. By the Jeans escape mechanism, to first-order

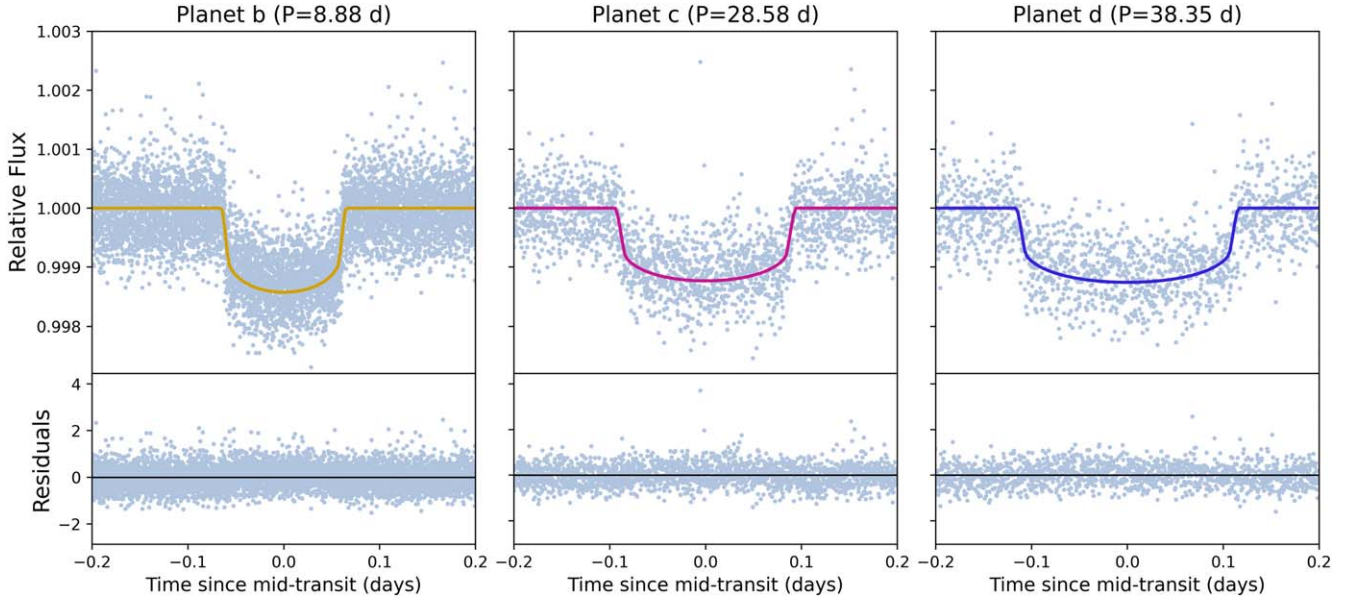


Figure 4. Phase-folded light curves for each of the transiting planets, with our best-fit model overlaid and residuals below.

approximation a gas will eventually completely escape if its thermal velocity exceeds one-sixth the planet’s escape velocity. Planet b’s temperature is likely high enough to allow the steady escape of atomic and molecular hydrogen. Fixing each planet’s radius to the median values of our photometry model, we calculated whether molecular hydrogen would escape each planet for a grid of every combination of planet mass and equilibrium temperature out to 3σ of each value. We find that molecular hydrogen escapes planet b in 84% of combinations, 52% for planet c, and 94% for planet d. Following the same procedure, planet d’s small mass means that it may not even be able to retain helium, as 47% of combinations allow this gas to escape. If any of these planets are experiencing atmospheric escape, transmission spectroscopy with JWST might show evidence.

5. Planet f Constraints

What is the nature of the fifth planet in the system? Our RV analysis favors both a trend and curvature in the residuals of the preferred four-planet model, suggesting a fifth planet with an orbital period much longer than our 415-day observing baseline. The presence of this planet can be further constrained by the change in HD191939’s proper motion over a period of 24 yr. Using these independent data sets, we can place constraints on the mass and semimajor axis of planet f.

We derived these constraints using a novel method that compares model orbits using just three free parameters. We quantify long-period signals in the RV residuals through trend ($\dot{\gamma}$) and curvature ($\ddot{\gamma}$) terms, and astrometric motion through $\Delta\mu$, the difference in proper motions at two epochs. We generated a set of randomly sampled orbits and computed these three parameters for each. A high-likelihood orbital model is one that reproduces the true values of $\dot{\gamma}$, $\ddot{\gamma}$, and $\Delta\mu$.

To produce a set of model orbits, we first defined our search range for both mass and semimajor axis. We started with τ_{\min} , the lower bound on orbital period. Planet f produced only a small detected curvature over our observing baseline, a feature that we estimate would require an orbital period $\gtrsim 4$ times the baseline. This yielded a lower semimajor axis limit of 2.6 au.

We limited our search to semimajor axes within 50 au. We used a similar argument to obtain a lower bound on M_p . We took the maximum ΔRV from the residuals of fitting for planets b–e and set it equal to the semiamplitude of a planet with a period of τ_{\min} , again assuming a circular orbit. From this amplitude, we calculated a minimum mass of $2.05 M_J$. We chose $200 M_J$ as the upper limit of our mass search, reasoning that more massive objects would be luminous enough to detect in high-contrast imaging.

We marginalized over four additional orbital parameters: inclination i , eccentricity e , argument of periastron ω , and mean anomaly M . In total we drew 10^8 random samples from this six-dimensional parameter space using the following prior distributions:

1. $\log\left(\frac{a}{1 \text{ au}}\right) \sim \mathcal{U}(2.62, 50)$
2. $\log\left(\frac{M_p}{1 M_J}\right) \sim \mathcal{U}(2.05, 200)$
3. $\cos(i) \sim \mathcal{U}(0, 1)$
4. $\omega \sim \mathcal{U}(0, 2\pi)$
5. $M \sim \mathcal{U}(0, 2\pi)$
6. $e \sim \mathcal{B}(0.867, 3.03)$

where \mathcal{B} is the two-parameter Kipping (2013) beta distribution for e . We used the same samples to generate both the RV curves and the astrometric proper motions.

To impose RV constraints, we computed for each sample the first ($\dot{\gamma}$) and second ($\ddot{\gamma}$) time derivatives of the stellar RV. We began by differentiating the true anomaly ν :

$$\nu = 2 \tan^{-1} \left(\sqrt{\frac{1+e}{1-e}} \tan\left(\frac{E}{2}\right) \right) \quad (1)$$

$$\dot{\nu} = \frac{2\pi\sqrt{1-e^2}}{\tau(1-e\cos(E))^2}, \quad (2)$$

where τ is the orbital period calculated from Kepler’s third law and E is the eccentric anomaly, which we obtained by

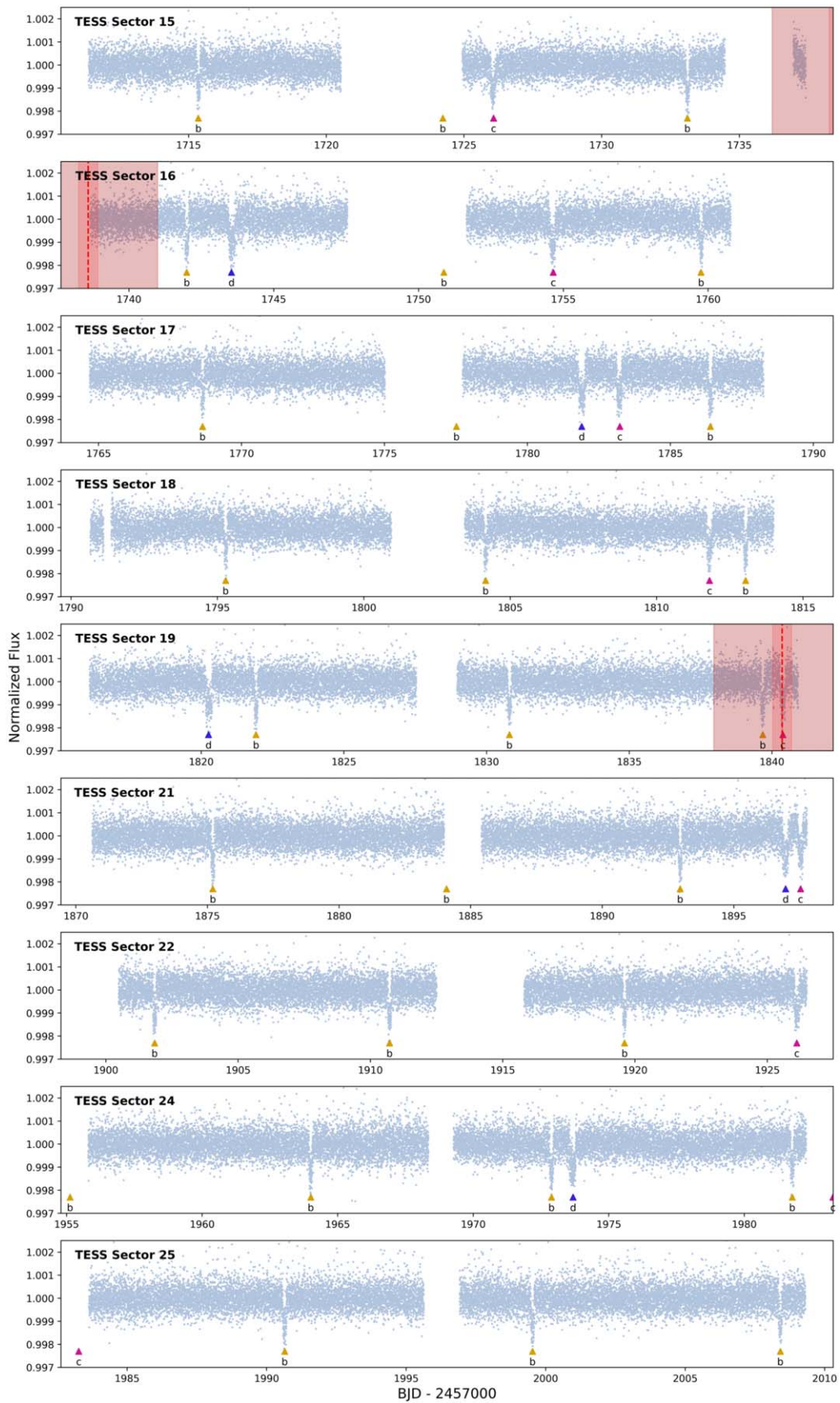


Figure 5. TESS photometry from sectors 15–19, 21, 22, 24, and 25, highlighting the transits of the three sub-Neptunes, which are indicated by color-coded arrows. Our RV model’s predicted transit midpoint times for planet e are shown by vertical dashed red lines, along with 3σ error windows as light-red shaded regions. The predicted ~ 8 hr transit duration (for a central transit) is shown by dark-red shading. An additional transit window occurred in Sector 23, when the star was not visible in any TESS cameras.

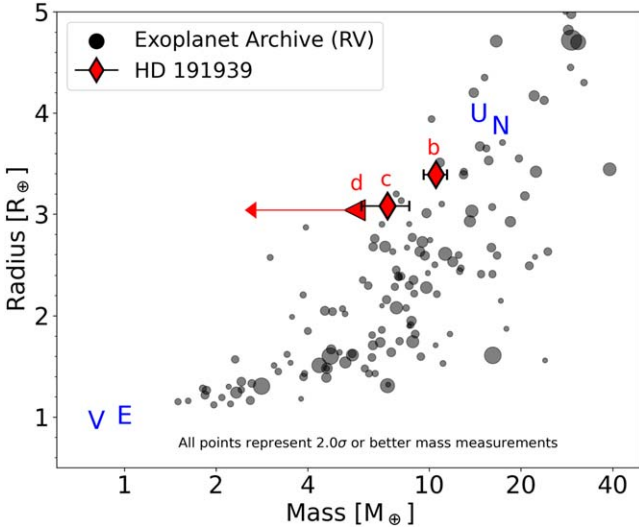


Figure 6. A mass–radius diagram highlighting the HD 19139 transiting planets. Larger marker sizes correspond to more precise mass measurements, excluding the HD 19139 planets. Planet d’s marker represents the 2σ upper limit, and its arrow points back to the median value. Gray points are from the NASA Exoplanet Archive as of 2021 July 1, with cuts to include only 2σ masses or better.

numerically solving Kepler’s equation:

$$M = E - e \sin E. \quad (3)$$

The second derivative of ν is also needed to compute $\ddot{\gamma}$:

$$\ddot{\nu} = -\dot{\nu}^2 \frac{2e \sin(E)}{\sqrt{1-e^2}}. \quad (4)$$

With the derivatives of ν , we can write the equations for $\dot{\gamma}$ and $\ddot{\gamma}$. We start with the RV value itself, γ :

$$\gamma = K[e \cos(\omega) + \cos(\nu + \omega)], \quad (5)$$

where

$$K = \sqrt{\frac{G}{1-e^2}} \frac{M_p \sin i}{\sqrt{a(M_p + M_*)}}. \quad (6)$$

The derivatives of γ are

$$\dot{\gamma} = -K[\dot{\nu} \sin(\nu + \omega)] \quad (7)$$

and

$$\ddot{\gamma} = -K[\dot{\nu}^2 \cos(\nu + \omega) + \ddot{\nu} \sin(\nu + \omega)]. \quad (8)$$

We evaluated the sample likelihood according to

$$P(\dot{\gamma}, \ddot{\gamma} | \dot{\gamma}_m, \ddot{\gamma}_m) \propto \exp \left[- \left(\frac{(\dot{\gamma} - \dot{\gamma}_m)^2}{2\sigma_{\dot{\gamma}}^2} + \frac{(\ddot{\gamma} - \ddot{\gamma}_m)^2}{2\sigma_{\ddot{\gamma}}^2} \right) \right]. \quad (9)$$

To obtain the 2D a – M_p joint posterior, we marginalized over $\{e, i, \omega, M\}$. The results from the RV-only constraints can be seen in Figure 7 in green with 1σ and 2σ contours.

We next incorporated astrometry to further constrain the characteristics of the fifth planet. Brandt (2021) aligned the reference frames of Hipparcos (ESA 1997) and Gaia EDR3 (Lindgren et al. 2021) to produce a self-consistent catalog of stellar proper motions measured at epochs 1991.25 and 2015.5. Brandt (2021) reported the proper motion based on the difference in position between these epochs. The Gaia and position-derived proper motions, $\vec{\mu}_G = (150.19 \pm 0.02, -63.99 \pm 0.02)$ mas yr $^{-1}$

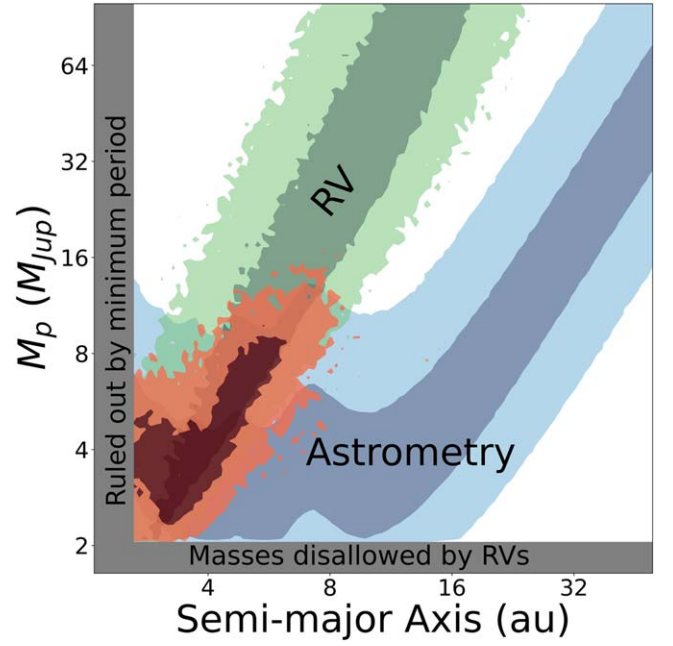


Figure 7. Constraints on the mass and semimajor axis of planet f. The green region shows values that are consistent with the measured RV trend and curvature. The blue region shows values that are consistent with the Hipparcos/Gaia astrometry. The red region shows the values consistent with both RV and astrometry. Dark and light regions indicate the 1σ and 2σ confidence intervals, respectively. Planet f is likely between 2 and 11 M_J , orbiting between 2.6 and 7.0 au.

and $\vec{\mu}_{HG} = (150.31 \pm 0.03, -63.94 \pm 0.03)$ mas yr $^{-1}$, were the most precise and indicated a change in proper motion $\Delta\mu = |\vec{\mu}_G - \vec{\mu}_{HG}|$ of 0.13 ± 0.03 mas yr $^{-1}$ over the 24 yr separating the two epochs.

Using the same orbit models as in the RV analysis, we first computed the average proper-motion vector in the Gaia EDR3 epoch. We also used the change in astrometric position between the Gaia and Hipparcos epochs to obtain an average proper motion over the 24 yr baseline. We then computed the magnitude of the difference vector $\Delta\mu_m$ and evaluated the likelihood via

$$P(\Delta\mu | \Delta\mu_m) \propto \exp \left(- \frac{(\Delta\mu - \Delta\mu_m)^2}{2\sigma_{\Delta\mu}^2} \right). \quad (10)$$

The detected proper-motion difference rules out high-mass models that were permitted by our RV-only analysis. The blue region of Figure 7 shows the range of a – M_p values that are allowed by astrometry at the 1σ and 2σ levels.

Because the RV and astrometric data sets are independent, we may evaluate the joint RV–astrometry likelihood by multiplying Equations (9) and (10). Figure 7 shows in red the region of a – M_p space that is allowed by both the RV and astrometric constraints. We find at 95% confidence that planet f has a mass of 2–11 M_J and orbits at a distance of 2.6–7.0 au.

Throughout this paper we refer to this companion as a “planet” because these current mass constraints place it most likely below the generally accepted upper mass limit for planets of $\sim 13 M_J$, but we caution that the high-mass tail of the probability distribution includes objects that would typically be characterized as brown dwarfs. Such high-mass objects on the planet–brown dwarf boundary are thought to form by one of two general formation pathways: core accretion

(Pollack et al. 1996) or gravitational instability (Boss 1997). Core accretion is more successful at producing low-mass objects and is the most plausible formation channel for planets b through e. Schlaufman (2018) showed a transition point in formation mechanism at $10 M_J$, which may represent a mass upper limit for objects formed via core accretion. Therefore, more massive objects more likely formed via gravitational instability and are therefore not planets. If planet f is at the upper end of its mass range, gravitational instability becomes a plausible pathway. This raises the possibility that both mechanisms were active in the HD 191939 system. We advocate for continued Doppler/astrometric monitoring of the HD 191939 system to fully resolve this companion’s orbit and measure its mass more precisely to identify which formation channel is more likely.

6. Planet e Is Nearly Coplanar

What is the inclination of planet e? Given the emergence of planet e in our RV data, we searched the TESS photometry for evidence of its transit. We would expect this $0.34 \pm 0.01 M_J / \sin i$ Jovian planet to have a radius of $\sim 1 R_J$, implying a transit depth on the order of 1%. At a 101-day orbital period, assuming zero eccentricity and an edge-on orbit, we expect the duration of its transit to be ~ 8 hr. Such a transit event should be obvious in the data by visual inspection. We do not see planet e’s transit (see Figure 5).

Within the error bars of our period and time of conjunction for planet e, it is possible that TESS missed the transits of planet e by unlucky timing. Still, the most likely explanation for the missing transits is that the planet is nontransiting. We did not search for a transit of planet f because its transit event should be a similar depth but even longer than planet e’s, and it was not near its expected time of conjunction at the time of TESS’s observations.

Assuming that planet e is nontransiting and has a radius of $1 R_J$, we place an upper limit on the inclination at 89.5° . To place a lower limit, we explored the dynamics of the system with Laplace–Lagrange secular perturbation theory (Marquis de Laplace 1825). Following the methods in Murray & Dermott (2010), we analytically derived equations for the time dependence of the inclination for each of the planets in the system. We chose to ignore effects from planet f. Due to planet f’s large semimajor axis relative to the other four planets, the inner four will move together under its influence. Additionally, any of the effects from planet f will play out over much longer timescales than we are interested in (~ 2 orders of magnitude longer). For the four planets in question, we used the median values for mass and semimajor axis from Table 1. Within the Laplace–Lagrange framework, eccentricity and inclination become decoupled; for simplicity and consistency with our preferred RV model, we assumed circular orbits.

The Laplace–Lagrange secular perturbation theory is built on the foundation of the disturbing function, where I is the inclination, and j and k are planet indices that run from 0 to N , with N being the number of planets in the system:

$$\frac{\partial I_j}{\partial t} = -\frac{1}{n_j a_j^2} \frac{\partial R_j}{\partial \Omega_j}, \quad (11)$$

where R_j is the disturbing function

$$R_j = n_j a_j^2 \left[\frac{1}{2} B_{jj} I_j^2 + B_{jk} I_j I_k \cos(\Omega_j - \Omega_k) \right], \quad (12)$$

with

$$B_{jk} = \frac{1}{4} \left[\frac{G(M_* + m_j)}{a_j^3} \right]^{\frac{1}{2}} \frac{m_k}{M_* + m_j} \alpha_{jk} \bar{\alpha}_{jk} b_{\frac{3}{2}}^{(1)}(\alpha_{jk}) \quad (13)$$

and

$$n_j = \sqrt{\frac{G(M_* + m_j)}{a_j^3}}, \quad (14)$$

where $B_{jk} = -B_{kj}$. Terms α_{jk} and $\bar{\alpha}_{jk}$ are constants determined by semimajor axis ratios of the j th and k th planets, $b_{\frac{3}{2}}^{(1)}(\alpha_{jk})$ is a definite integral also dependent on semimajor axes (Murray & Dermott 2010), and Ω is the longitude of ascending node. From the disturbing function we constructed the B matrix. The eigenvalues of the B matrix, f_k , represent the periodicity of the oscillations of the planets’ inclination, and the eigenvectors (which are unscaled and must be normalized), along with the initial conditions of the system’s configuration, represent the amplitude of the oscillations.

In the normalization process we calculated both a scaling factor and a phase angle for the oscillation periodicity of each planet, γ_k . This is accomplished by implementing the initial conditions at $t=0$ (both I_o and Ω_o) to generate a set of $2N$ equations from which we can solve for N scaling factors and N phase angles. With these scaling factors in hand, the final amplitudes of the oscillations, V_{jk} , are determined.

Then, we calculated the inclinations of each planet at a given time:

$$I_j = (p_j^2 + q_j^2)^{\frac{1}{2}}, \quad (15)$$

where p_j and q_j are parameterized variables,

$$p_j = \sum_{k=0}^{N_{\text{planets}}} V_{jk} \sin(f_k t + \gamma_k), \quad (16)$$

$$q_j = \sum_{k=0}^{N_{\text{planets}}} V_{jk} \cos(f_k t + \gamma_k). \quad (17)$$

Within this framework, we derived $I_j(t)$ for each planet $j \in \{b, c, d, e\}$ for various initial configurations of the system.

For each configuration, planets b, c, and d were initialized at 0° , corresponding to placing all three on the same plane. Note that the plane from which we are measuring inclinations is 90° transposed from the conventional plane of reference for inclinations, the sky plane. For ease of reference, we call this plane the LL plane. We also initialized all four planets’ longitude of ascending node, Ω , to the same value, arbitrarily 0° . We tested various trials where Ω_e was initialized at different values between 0° and 360° and found that it had little to no effect on the outcome of our experiment. In each configuration we set the starting inclination for planet e to different values, stepping in 0.5° intervals from 0° to 12° .

We computed $I_j(t)$ for an 8000 yr span, roughly double the longest eigenfrequency. For every year in a configuration, we

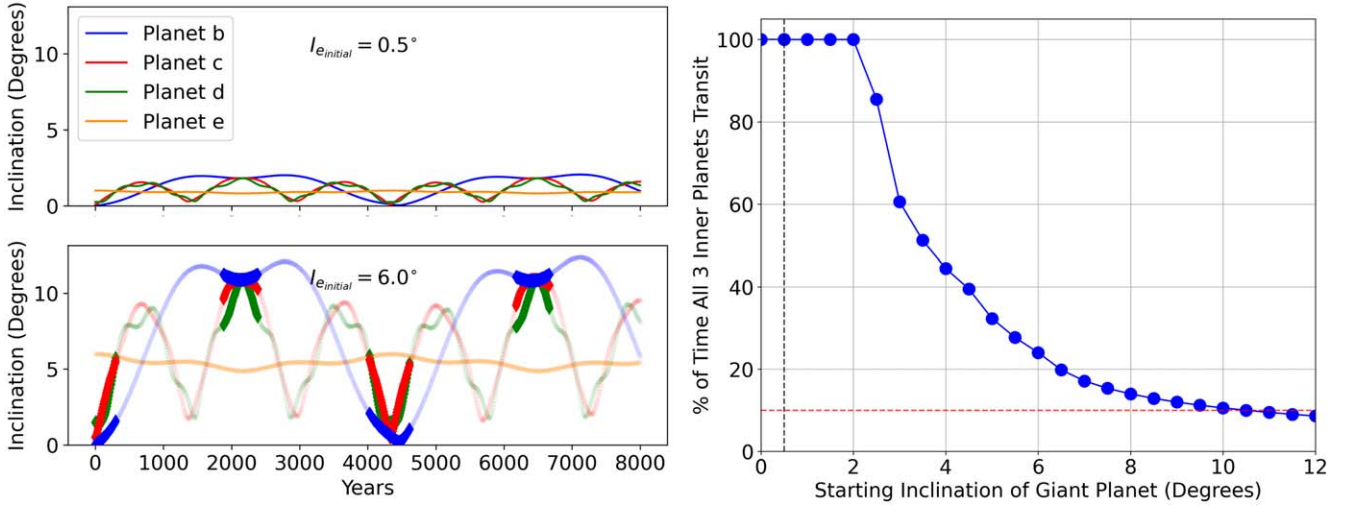


Figure 8. Details on the Laplace–Lagrange analysis. Left: the inclination curves for each planet when planet e is given a starting value of $I_e = 0.5^\circ$ vs. $I_e = 6.0^\circ$. When the mutual inclination of the three is small enough for all three to transit together, the line is opaque. Right: the percent of time during which the inner three planets transit depends on the inclination of planet e. The vertical black dashed line indicates the nominal maximum inclination for which we would expect planet e to still transit. The horizontal red dashed line indicates the 10% threshold for our conservative estimate on the upper limit to the giant planet’s inclination.

computed the mutual inclination of the three planets:

$$\cos I_{xy} = \cos I_x \cos I_y + \sin I_x \sin I_y \cos(\Omega_x - \Omega_y) \quad (18)$$

(Carter et al. 2012). We determined a maximum limiting angle for mutual transiting of the inner three planets by geometric reasoning. We calculated the minimum transiting inclinations for both the innermost and second-innermost planets, by $i_{\min} \approx \frac{R_*}{a}$. Then, the sum of these two angles is the limiting angle. This corresponds to placing the innermost and second-innermost planets at the opposite limbs of the star. For a given time stamp, if the mutual inclinations of all pairs of planets are less than the limiting angle, then all planets transit together at that time stamp.

Figure 8 shows the $I_j(t)$ curves for two examples from our trials, as well as the results of all trials. For each trial of planet e’s starting inclination, we computed the percent of time stamps within the 8000 yr time span, during which all three of the inner planets transited with respect to an arbitrary line of sight. As expected, the farther from the LL plane that we start planet e’s inclination, the smaller the percent of the time stamps during which all three inner planets will transit. There is a range of starting inclinations for which we would expect all three inner planets to transit 100% of the time stamps, from 0° to 2.0° in the LL plane. We nominally rule out inclinations less than 0.5° based on the absence of a transit for planet e, although this limit does not take into account the uncertainty in planet e’s radius and the simplification that all three inner planets start at 0° . In sample tests where we included planet f with mass and semimajor axis values drawn from results in Section 5, we find the results to be similar. Including planet f, the value for the percentage of time stamps where the inner three planets are all transiting for any given inclination of planet e is within 5% of the value when we exclude planet f.

Above 2.0° in the LL plane, the percentage of time stamps where all three are transiting together falls sharply and then decreases asymptotically toward 0%. From these results, we conservatively place an upper limit on planet e’s mutual inclination at 10° . This angle corresponds to a lower limit for absolute inclination of 80° in the conventional sky-plane frame

of reference. For starting inclinations above 10° , the amplitudes of the planets’ oscillations in inclination space become large enough that it is rare for all three to transit together from an arbitrary line of sight: $<10\%$ of the time stamps tested. Mutual inclinations of planet e larger than 10° are viable solutions. However, in those scenarios, the decreasingly short windows in time where all three planets transit make Earth observers increasingly lucky to have caught the system at one of these rare moments in its dynamical periodicity. This investigation suggests that planet e is likely to be nearly coplanar with the three transiting planets.

7. TTVs and MMR

Planets c and d have orbital periods very near to 4:3 mean motion resonance (MMR). But do they indeed reside in MMR? We explored this possibility and the implications that follow.

In general, planets that reside in MMR are characterized by period ratios of

$$\frac{P_2}{P_1} = \frac{j}{j-1}, \quad (19)$$

where j is an integer and subscripts 1 and 2 denote the inner and outer planet of the pair, respectively. We quantify the “proximity” to MMR by

$$\Delta_{12} = \frac{P_2 j - 1}{P_1 j} - 1, \quad (20)$$

following Lithwick et al. (2012).

Applying this formula to planets c and d, $\Delta_{cd} = 0.6432\% \pm 0.0001\%$. Following Batygin & Adams (2017), the resonant bandwidth can be approximated as

$$|\chi| \lesssim 5 \frac{j-1}{j^{2/3}} \left(\frac{M_1 + M_2}{M_*} \right)^{2/3}. \quad (21)$$

For planets c and d, $\chi_{cd} = 0.662\% \pm 0.001\%$. Because $\Delta < |\chi|$, we cannot rule out that the two planets are librating in MMR.

Under the assumption that planets c and d are close to but *not* in MMR, we calculated the period and amplitude of TTV

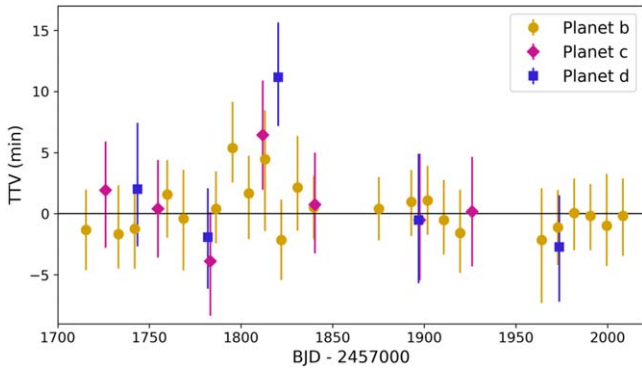


Figure 9. TTVs of the transiting planets over the duration of the TESS photometry. We do not detect significant TTVs for any of the transiting planets over the observing baseline.

oscillations of the pair following Lithwick et al. (2012). TTV oscillations will be oppositely phased sinusoids, each at a period designated as the *super-period* (SP):

$$P_{\text{SP}} = \frac{P_2}{j|\Delta|}, \quad (22)$$

with amplitudes

$$\text{TTV}_1 = P_1 \frac{\left(\frac{m_2}{M_*}\right)}{\pi j^{2/3} (j-1)^{1/3} \Delta} \left(-f - \frac{3Z}{2\Delta}\right) \quad (23)$$

and

$$\text{TTV}_2 = P_2 \frac{\left(\frac{m_1}{M_*}\right)}{\pi j \Delta} \left(-g - \frac{3Z}{2\Delta}\right), \quad (24)$$

where f and g are constants associated with the MMR ratio, in this case 4:3, and Z is a linear combination of the free eccentricities of the two planets.

We calculated the SP of planets c and d to be 1490 ± 10 days. In the circular orbit limit, $Z = 0$ and the amplitudes of planet c and d’s TTV oscillations are 15.5 ± 9.1 minutes and 59.2 ± 13.8 minutes, respectively. If the phase of the oscillations is near an inflection point, Planet d’s oscillation would be large enough that it could be detected even though TESS has only sampled about one-fifth of the SP.

To further investigate, we calculated the TTV associated with each transit event. We generated model transits offset from the expected transit time by between ± 60 minutes and calculated the chi-squared (χ^2) fit of these model transits to the light curve. We adopted the offset that minimized the χ^2 statistic as the value of the TTV. The 1σ error bars are calculated from the offset where the χ^2 increased from its minimum value by 1.0. We performed this process for each transit of each planet.

Figure 9 and Table 3 show all of the TTVs for each planet. Planet d’s five transits cover ~ 230 days of time, or about 15% of the SP. Its TTVs do not show a trend. Planet c’s transits similarly span only ~ 230 days. Due to TESS’s observing strategy, planet c transited just hours before sector 24 observations and hours before and after sector 25 observations, at times when the star was not visible to TESS. It is noteworthy that the two planets behave similarly in that when one is late, the corresponding transit of the other is similarly late and

vice versa for early transits. Planet b’s TTVs are consistent with zero, showing no trend or significant sinusoidal variation.

These results can be interpreted in two ways. First, and most likely, TESS has not sampled enough of the 1500-day SP to make a conclusive finding. Alternatively, we could be sampling TTVs very near the maximum or minimum of the TTV signal’s phase, so the ΔTTV over the baseline is too small for a significant detection. TESS’s extended mission cycle 4 will shed more light on these three possibilities.

8. Gap Complexity

Could there be an additional planet hiding in the gap between planets b and c? With planets c and d very near MMR, it is noticeable that there are not more pairs of planets also spaced in near-resonant orbits. Following the peas-in-a-pod architecture where multiplanet systems show similarly sized planets in regular orbital distance spacing, we might expect more than just one pair in this system to exhibit near resonance, especially considering that the transiting planets have very similar radii (Leleu et al. 2021).

In the residuals of our GLS periodogram (Figure 1), there is a noticeable peak between planets b and c at 17.7 days. A planet at this period would be particularly interesting, as it would be near 2:1 resonance with planet b and 8:5 resonance with planet c. A planet at this period would also fill the gap in log period space of this system well. Given that we have a strong RV detection of planet c, any additional planet in this gap between planets b and c must be less massive than planet c and inclined. When we add a fit for a 17.7-day planet in our preferred model, we find a 2σ upper limit to its mass to be $6 M_{\oplus}$. In order to be nontransiting, its inclination must be at least 2° from the LL plane.

We followed the methods in Gilbert & Fabrycky (2020) to calculate the gap complexity, \mathcal{C} , for the HD 191939 system. \mathcal{C} describes the deviation from uniform planet spacing in a system. $\mathcal{C} = 0$ indicates uniform spacing in log period space, while as $\mathcal{C} \rightarrow 1$ the less uniform the spacing. For Kepler systems, \mathcal{C} peaks at 0, with the majority ($\sim 75\%$) of systems having $\mathcal{C} < 0.2$. Systems with larger \mathcal{C} values are more likely to have additional planets hiding in the gaps between known planets. We calculate $\mathcal{C}_{\text{HD191939}} = 0.846$ considering the transiting planets only, as planet e does not fall into the peas-in-a-pod configuration. We interpret the high value of \mathcal{C} to mean that there is a significant gap, which could be the site of an additional planet. When we include a hypothetical planet on a 17.7-day period with the known transiting planets, we calculate $\mathcal{C}_{\text{HD191939}} = 0.18$. This value is consistent with the findings of Gilbert & Fabrycky (2020) for the general pattern of multiplanet system configurations. Adding a 17.7-day planet to our preferred model does not improve the likelihood enough to justify the extra three parameters. Nevertheless, this planet candidate is interesting and deserves continued attention with additional RV observations.

9. Follow-up Prospects

How well suited is this system for further follow-up? We identified HD 191939 as a key TKS target for atmospheric follow-up with the target selection algorithm described in Scarsdale et al. (2021). As a bright ($J = 7.6$ mag) multiplanet system, space-based spectroscopic observations offer a unique opportunity for studies in planet formation and evolution.

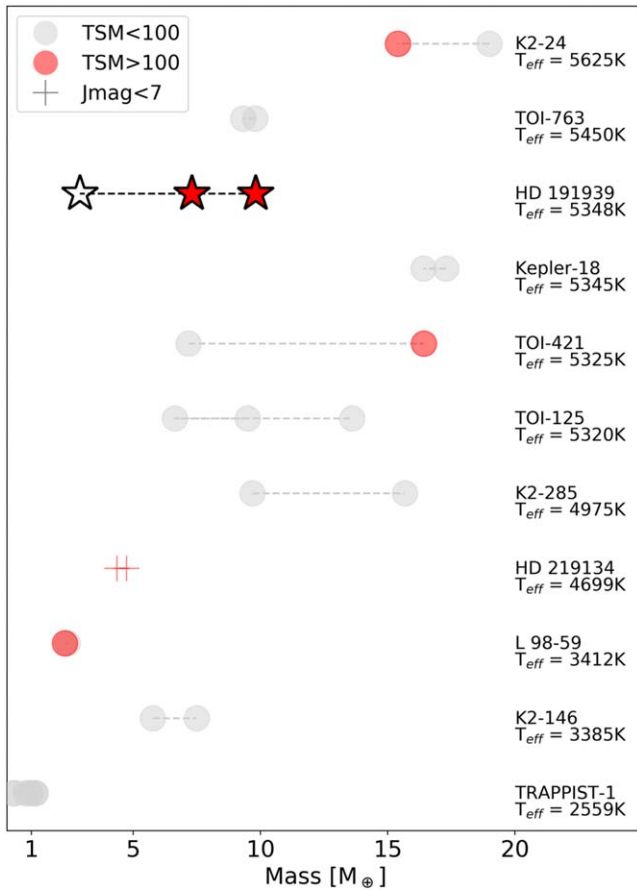


Figure 10. All multiplanet systems with 5σ masses and radii for small planets ($R_p < 10 R_\oplus$, $M_p < 100 M_\oplus$) with TSMs > 20 . Planets are plotted by mass and arranged vertically in order of host star effective temperature (hotter at the top). HD 191939 b and c have TSM values that are individually among the best in the sub-Neptune population and are unique in having the same host star. Due to planet d’s weak mass measurement, it appears in this plot unfilled. HD 191939 is the only system to date with multiple planets with TSMs greater than 100 that also does not saturate JWST.

We use the Transmission Spectroscopy Metric (TSM; Kempton et al. 2018) to quantify the expected S/N of JWST-NIRISS observations for the transiting planets:

$$\text{TSM}_p = S \times \frac{R_p^3 T_{\text{eq}}}{M_p R_*^2} \times 10^{-0.2m_j}, \quad (25)$$

where S is a dimensionless normalization constant, equal to 1.28 for planets $2.75 R_\oplus < R_p < 4.0 R_\oplus$. The TSM is a proxy for the expected S/N from a 10 hr observing program with JWST-NIRISS assuming a cloud-free, solar-metallicity, H_2 -dominated atmosphere. For reference, HD 3167c, a sub-Neptune orbiting an early K dwarf with a recent water vapor detection from five HST-WFC3 transits (Mikal-Evans et al. 2021), has a TSM of about 100.

Using the derived planet parameters from Table 1, we find that HD 191939 b has a TSM of 151 ± 18 , which places it in the top quartile of targets in the $2.75 R_\oplus < R_p < 4.0 R_\oplus$ range from the statistical sample in Kempton et al. (2018). HD 191939c has a TSM of 106 ± 24 , placing it in the third quartile from the top of TSM values for planets between 2.75 and $4.0 R_\oplus$. We place a lower limit on the TSM of planet d, finding $\text{TSM}_d > 72$ at 2σ confidence. The HD 191939 system is the

only system which does not saturate JWST with multiple small planets with five sigma masses and TSM’s greater than 100, see Figure 10. For the transit durations reported in Table 1, our TSM values scale to an expected single-transit S/N with JWST-NIRISS of 84 ± 10 , 71 ± 16 , and > 53 for planets b, c, and d, respectively, where the lower limit for planet d represents 2σ confidence.

We used PandExo (Batalha et al. 2017) to estimate the nominal heights of molecular features in a single-transit JWST-NIRISS transmission spectrum for planet b, assuming a cloud-free, solar-metallicity atmosphere. In this ideal case we find feature heights of ~ 100 – 300 ppm between 1 and $5 \mu\text{m}$. In reality, clouds and/or enhanced atmospheric metallicity will probably reduce these amplitudes by a factor of three or more (Wakeford et al. 2019). Additionally a subsolar C/O ratio, which may be implied from the host star’s abundance measurements, also disagrees with the ideal case of a solar-metallicity composition and would produce spectra dominated by CO, H_2O , and CO_2 .

A spin-orbit measurement for this system would be particularly informative to planetary formation theories. Only eight systems with three or more planets have had their sky-projected obliquity angles, λ , measured. In the HD 191939 system, the three inner planets all lie in nearly the same orbital plane, while we have shown that the giant planet should lie close to this plane. If they are misaligned with respect to the stellar spin axis, that could inform the dynamical history of the system and the roles that planets e and f have played in shaping the system. However, the low $v \sin i$ (see Table 1) of the host star might be prohibitive to a Rossiter–McLaughlin (RM; Rossiter 1924; McLaughlin 1924; Gaudi & Winn 2007) measurement of even the largest expected signal from planet b. A simulation using *arome* (Boué et al. 2013) finds that for $v \sin i = 1 \text{ km s}^{-1}$ and $\lambda = 0^\circ$, planet b’s expected RM amplitude is 1.5 m s^{-1} .

HD 191939 will be observed again by TESS in Cycle 4. Nominal dates for observations include six sectors of additional coverage: 41, 48, 49, 51, 52, and 55. These observations will extend the total baseline of photometry observations to 2022-09-01 for a total of 1142 days, about 76% of the SP between planets c and d.

10. Conclusions

The overall architecture of the HD 191939 system—multiple small planets, then a warm Saturn, followed by a high-mass planet—seemingly stands alone among known systems. Sub-Neptunes are nearly ubiquitous (Howard et al. 2012; Petigura et al. 2013), but the a priori occurrence rate for warm sub-Jovians (30 – $300 M_\oplus$ at 0 – 1.0 au) is much smaller at $\sim 3\%$, and similarly at $\sim 5\%$ for cold super-Jovians (300 – $6000 M_\oplus$ at 3 – 10 au; Fulton et al. 2021). We cannot simply multiply together these occurrence rates to discern how rare it is for such a system like HD 191939 to exist, as Weiss et al. (2018) found that adjacent planets tend to have similar sizes, and some studies have found a relationship between sub-Neptune occurrence and giant planet occurrence (Zhu & Wu 2018; Bryan et al. 2019).

We searched the literature for analog systems by performing cuts on the known population for systems with four planets, with three sub-Neptunes ($M_p < 25 M_\oplus$) interior to a warm Saturn ($50 M_\oplus < M_p < 300 M_\oplus$, with orbital period of 50 – 360

days) and a long-period high-mass planet. However, there are a few systems that stand out as notable.

Mills et al. (2019) describe three systems, Kepler-65, Kepler-68, and Kepler-25, with high-mass outer planets. Kepler-65 has a tight inner system of three sub-Neptunes and a $0.28 M_J$ planet with an orbital period of 258 days, similar to the inner system of HD 191939, but there is no evidence for a trend over a ~ 2000 -day baseline. Kepler-25 is similar in having two inner sub-Neptunes in/near resonance (2:1) and a Saturn-mass planet at just over a 100-day orbit, but, again, no evidence for a long-period companion represented by trend over its ~ 3000 -day observing baseline. Kepler-68 may represent the most similar system to HD 191939. It has an inner system of two sub-Neptunes, then a Jovian with an orbital period of 634 days, and then strong evidence for curvature in the residuals. Mills et al. (2019) attribute this curvature to an object with a period much longer than the ~ 3000 -day baseline and place a lower limit of $0.6 M_J$, but no upper limit. Lastly, Kepler-129 (Zhang et al. 2021) bears resemblance to HD 191939 in having two inner planets at $< 45 M_\oplus$ and a high-mass Jovian ($8.3 M_J$) on a ~ 7 yr orbit. Zhang et al. (2021) also discuss the perturbations of inclinations of the inner transiting planets due to the long-period Jovian. Each of these systems has pieces of the HD 191939 system, but none have the full architecture.

Bright, multiplanet systems are invaluable to the exoplanet community owing to their enhanced follow-up opportunities and comparative planet prospects. With photometry from TESS and RV data from both Keck/HIRES and the APF, we have characterized the HD 191939 system: three transiting sub-Neptune planets, a fourth Jovian, and a fifth high-mass planet. We have measured the planets' masses, as well as their radii and densities where applicable. Because of our strong mass measurements of three of the four inner planets ($> 5\sigma$), we are able to explore and further investigate many aspects of the system to answer more detailed questions about the system. Our main conclusions are as follows:

1. The bulk densities of the transiting planets are $\rho_b = 1.5 \pm 0.2 \text{ g cm}^{-3}$, $\rho_c = 1.4 \pm 0.3 \text{ g cm}^{-3}$, and $\rho_d = 0.5 \pm 0.3 \text{ g cm}^{-3}$. We find that the compositions of the planets are best explained by extended H/He atmospheres.
2. By a new technique for constraining the mass and period of distant companions using both RV and astrometric data sets, we find planet f to be between 2 and $11 M_J$ on a 1700-to-7200-day orbital period at 95% confidence.
3. Through a dynamical analysis using Laplace–Lagrange secular perturbation theory, we constrain the inclination of the nontransiting planet e. We find that it most likely orbits within a plane less than 10° from the plane roughly shared by the three transiting planets.
4. By investigation into the potential mean motion resonance of planets c and d, we predict their TTV amplitudes to be 15.5 ± 9.1 minutes and 59.2 ± 13.8 minutes, respectively, over an SP of 1490 ± 10 days. However, we find no evidence for significant TTVs over the short observing baseline (326 days) compared to the SP of the interaction (1500 days).
5. We analyze the RV residuals and the gap complexity of the system to investigate the potential for additional planets in the system, identifying a possible planet candidate at 17.7 days that deserves continued attention.
6. We evaluate the transiting planets' prospects for atmospheric characterization through transmission spectroscopy

with JWST. HD 191939 is the only system that does not saturate JWST-NIRISS where two planets both have TSMs greater than 100, making it an excellent candidate for comparative atmospheric studies.

With its three transiting mini-Neptunes, one nontransiting Jovian planet, and distant high-mass planet surrounding a bright, nearby host star, HD 191939 provides a rich natural laboratory for detailed atmospheric characterization and dynamical studies.

We thank the anonymous referee for their insightful and thorough comments. We are grateful to Tim Brandt for his insight and contributions to the methods of Section 5. We thank the time assignment committees of the University of California, the California Institute of Technology, NASA, and the University of Hawai'i for supporting the TESS-Keck Survey with observing time at Keck Observatory and on the Automated Planet Finder. We thank NASA for funding associated with our Key Strategic Mission Support project. We gratefully acknowledge the efforts and dedication of the Keck Observatory staff for support of HIRES and remote observing. We recognize and acknowledge the cultural role and reverence that the summit of Maunakea has within the indigenous Hawaiian community. We are deeply grateful to have the opportunity to conduct observations from this mountain. We thank Ken and Gloria Levy, who supported the construction of the Levy Spectrometer on the Automated Planet Finder. We thank the University of California and Google for supporting Lick Observatory and the UCO staff for their dedicated work scheduling and operating the telescopes of Lick Observatory. This paper is based on data collected by the TESS mission. Funding for the TESS mission is provided by the NASA Explorer Program. We acknowledge the use of public TESS data from pipelines at the TESS Science Office and at the TESS Science Processing Operations Center. This paper includes data collected by the TESS mission that are publicly available from the Mikulski Archive for Space Telescopes (MAST).

E.A.P. acknowledges the support of the Alfred P. Sloan Foundation. L.M.W. is supported by the Beatrice Watson Parrent Fellowship and NASA ADAP grant 80NSSC19K0597. A.C. acknowledges support from the National Science Foundation through the Graduate Research Fellowship Program (DGE 1842402). D.H. acknowledges support from the Alfred P. Sloan Foundation, the National Aeronautics and Space Administration (80NSSC18K1585, 80NSSC19K0379), and the National Science Foundation (AST-1717000). I.J.M.C. acknowledges support from the NSF through grant AST-1824644. P.D. acknowledges support from a National Science Foundation Astronomy and Astrophysics Postdoctoral Fellowship under award AST-1903811. A.B. is supported by the NSF Graduate Research Fellowship, grant No. DGE 1745301. R.A.R. is supported by the NSF Graduate Research Fellowship, grant No. DGE 1745301. C.D.D. acknowledges the support of the Hellman Family Faculty Fund, the Alfred P. Sloan Foundation, the David & Lucile Packard Foundation, and the National Aeronautics and Space Administration via the TESS Guest Investigator Program (80NSSC18K1583). J.M.A.M. is supported by the NSF Graduate Research Fellowship, grant No. DGE-1842400. J.M.A.M. also acknowledges the LSSTC Data Science Fellowship Program, which is funded by LSSTC, NSF Cybertraining grant No. 1829740, the Brinson

Foundation, and the Moore Foundation; his participation in the program has benefited this work. M.R.K is supported by the NSF Graduate Research Fellowship, grant No. DGE 1339067.

Facilities: Automated Planet Finder (Levy), Keck I (HIRES), TESS.

Software: Astropy (Astropy Collaboration et al. 2013), corner.py (Foreman-Mackey 2016), emcee (Foreman-Mackey et al. 2013), isoclassify (Huber et al. 2017), Jupyter (Kluyver et al. 2016), KeckSpec (Rice & Brewer 2020) matplotlib (Hunter 2007), numpy (Van Der Walt et al. 2011), pandas (McKinney 2010), Python Limb Darkening Toolkit (Parviainen & Aigrain 2015) RadVel (Fulton et al. 2018), Smint (Piaulet et al. 2021) SpecMatch-Syn (Petigura et al. 2017) Transit Least Squares (Hippke & Heller 2019) exoplanet (Foreman-Mackey et al. 2020a) and its dependencies (Agol et al. 2020; Astropy Collaboration et al. 2018; Espinoza 2018; Luger et al. 2019; Salvatier et al. 2016; Theano Development Team 2016).

ORCID iDs

Jack Lubin  <https://orcid.org/0000-0001-8342-7736>
 Judah Van Zandt  <https://orcid.org/0000-0002-4290-6826>
 Rae Holcomb  <https://orcid.org/0000-0002-5034-9476>
 Lauren M. Weiss  <https://orcid.org/0000-0002-3725-3058>
 Erik A Petigura  <https://orcid.org/0000-0003-0967-2893>
 Paul Robertson  <https://orcid.org/0000-0003-0149-9678>
 Joseph M. Akana Murphy  <https://orcid.org/0000-0001-8898-8284>
 Nicholas Scarsdale  <https://orcid.org/0000-0003-3623-7280>
 Konstantin Batygin  <https://orcid.org/0000-0002-7094-7908>
 Alex S. Polanski  <https://orcid.org/0000-0001-7047-8681>
 Natalie M. Batalha  <https://orcid.org/0000-0002-7030-9519>
 Courtney Dressing  <https://orcid.org/0000-0001-8189-0233>
 Benjamin Fulton  <https://orcid.org/0000-0003-3504-5316>
 Andrew W. Howard  <https://orcid.org/0000-0001-8638-0320>
 Daniel Huber  <https://orcid.org/0000-0001-8832-4488>
 Howard Isaacson  <https://orcid.org/0000-0002-0531-1073>
 Stephen R. Kane  <https://orcid.org/0000-0002-7084-0529>
 Arpita Roy  <https://orcid.org/0000-0001-8127-5775>
 Corey Beard  <https://orcid.org/0000-0001-7708-2364>
 Sarah Blunt  <https://orcid.org/0000-0002-3199-2888>
 Ashley Chontos  <https://orcid.org/0000-0003-1125-2564>
 Fei Dai  <https://orcid.org/0000-0002-8958-0683>
 Paul A. Dalba  <https://orcid.org/0000-0002-4297-5506>
 Steven Giacalone  <https://orcid.org/0000-0002-8965-3969>
 Michelle L. Hill  <https://orcid.org/0000-0002-0139-4756>
 Andrew Mayo  <https://orcid.org/0000-0002-7216-2135>
 Teo Močnik  <https://orcid.org/0000-0003-4603-556X>
 Molly R. Kosiarek  <https://orcid.org/0000-0002-6115-4359>
 Malena Rice  <https://orcid.org/0000-0002-7670-670X>
 Ryan A. Rubenzahl  <https://orcid.org/0000-0003-3856-3143>
 David W. Latham  <https://orcid.org/0000-0001-9911-7388>
 S. Seager  <https://orcid.org/0000-0002-6892-6948>
 Joshua N. Winn  <https://orcid.org/0000-0002-4265-047X>

References

Agol, E., Luger, R., & Foreman-Mackey, D. 2020, *AJ*, 159, 123
 Akaike, H. 1974, *ITAC*, 19, 716
 Astropy Collaboration, Price-Whelan, A. M., Sipőcz, B. M., et al. 2018, *AJ*, 156, 123
 Astropy Collaboration, Robitaille, T. P., Tollerud, E. J., et al. 2013, *AAP*, 558, A33
 Badenas-Agusti, M., Günther, M. N., Daylan, T., et al. 2020, *AJ*, 160, 113
 Batalha, N. E., Mandell, A., Pontoppidan, K., et al. 2017, *PASP*, 129, 064501

Batygin, K., & Adams, F. C. 2017, *AJ*, 153, 120
 Berger, T. A., Huber, D., van Saders, J. L., et al. 2020, *AJ*, 159, 280
 Boss, A. P. 1997, *Sci*, 276, 1836
 Boué, G., Montalto, M., Boisse, I., Oshagh, M., & Santos, N. C. 2013, *A&A*, 550, A53
 Brandt, T. D. 2021, *ApJS*, 254, 42
 Brewer, J. M., & Fischer, D. A. 2017, *ApJ*, 840, 121
 Bryan, M. L., Knutson, H. A., Lee, E. J., et al. 2019, *AJ*, 157, 52
 Butler, R. P., Marcy, G. W., Williams, E., et al. 1996, *PASP*, 108, 500
 Carter, J. A., Agol, E., Chaplin, W. J., et al. 2012, *Sci*, 337, 556
 Choi, J., Dotter, A., Conroy, C., et al. 2016, *ApJ*, 823, 102
 Chontos, A., Akana Murphy, J. M., MacDougall, M. G., et al. 2021, arXiv:2106.06156
 Dai, F., Roy, A., Fulton, B., et al. 2020, *AJ*, 160, 193
 Dalba, P. A., Gupta, A. F., Rodriguez, J. E., et al. 2020, *AJ*, 159, 241
 ESA 1997, ESA SP-1200, The HIPPARCOS and TYCHO Catalogues (Noordwijk: ESA)
 Espinoza, N. 2018, *RNAAS*, 2, 209
 Foreman-Mackey, D. 2016, *JOSS*, 1, 24
 Foreman-Mackey, D., Hogg, D. W., Lang, D., & Goodman, J. 2013, *PASP*, 125, 306
 Foreman-Mackey, D., Luger, R., Czekala, I., et al. 2020a, exoplanet-dev/exoplanet v0.3.2, Zenodo, doi:10.5281/zenodo.1998447
 Foreman-Mackey, D., Luger, R., Czekala, I., et al. 2020b, exoplanet-dev/exoplanet v0.4.1, Zenodo, doi:10.5281/zenodo.1998447
 Fulton, B. J., & Petigura, E. A. 2018, *AJ*, 156, 264
 Fulton, B. J., Petigura, E. A., Blunt, S., & Sinukoff, E. 2018, *PASP*, 130, 044504
 Fulton, B. J., Petigura, E. A., Howard, A. W., et al. 2017, *AJ*, 154, 109
 Fulton, B. J., Rosenthal, L. J., Hirsch, L. A., et al. 2021, *ApJS*, 255, 14
 Gaia Collaboration, Brown, A. G. A., Vallenari, A., et al. 2018, *A&A*, 616, A1
 Gaudi, B. S., & Winn, J. N. 2007, *ApJ*, 655, 550
 Gilbert, G. J., & Fabrycky, D. C. 2020, *AJ*, 159, 281
 Hippke, M., & Heller, R. 2019, *A&A*, 623, A39
 Howard, A. W., Johnson, J. A., Marcy, G. W., et al. 2010, *ApJ*, 721, 1467
 Howard, A. W., Marcy, G. W., Bryson, S. T., et al. 2012, *ApJS*, 201, 15
 Huber, D., Zinn, J., Bojsen-Hansen, M., et al. 2017, *ApJ*, 844, 102
 Hunter, J. D. 2007, *CSE*, 9, 90
 Isaacson, H., & Fischer, D. 2010, *ApJ*, 725, 875
 Jenkins, J. M., Twicken, J. D., McCauliff, S., et al. 2016, *Proc. SPIE*, 9913, 99133E
 Jontof-Hutter, D., Lissauer, J. J., Rowe, J. F., & Fabrycky, D. C. 2014, *ApJ*, 785, 15
 Kempton, E. M. R., Bean, J. L., Louie, D. R., et al. 2018, *PASP*, 130, 114401
 Kipping, D. M. 2013, *MNRAS*, 434, L51
 Kluyver, T., Ragan-Kelley, B., Pérez, F., et al. 2016, in Positioning and Power in Academic Publishing: Players, Agents and Agendas, ed. F. Loizides, B. Schmidt, & I. O. S. Press (Amsterdam: IOS Press), 87, <https://eprints.soton.ac.uk/403913/>
 Lee, E. J., & Chiang, E. 2016, *ApJ*, 817, 90
 Leleu, A., Alibert, Y., Hara, N. C., et al. 2021, *A&A*, 649, A26
 Lindgren, L., Klioner, S. A., Hernández, J., et al. 2021, *A&A*, 649, A2
 Lithwick, Y., Xie, J., & Wu, Y. 2012, *ApJ*, 761, 122
 Lopez, E. D., & Fortney, J. J. 2014, *ApJ*, 792, 1
 Luger, R., Agol, E., Foreman-Mackey, D., et al. 2019, *AJ*, 157, 64
 Marquis de Laplace, P.-S. 1825, *Traite de Mecanique Celeste* (Delhi: Facsimile Publisher), 569
 Masuda, K. 2014, *ApJ*, 783, 53
 McKinney, W. 2010, in Proc. 9th Python in Science Conf., ed. S. van der Walt & J. Millman, 51
 McLaughlin, D. B. 1924, *ApJ*, 60, 22
 Mikal-Evans, T., Crossfield, I. J. M., Benneke, B., et al. 2021, *AJ*, 161, 18
 Millholland, S. 2019, *ApJ*, 886, 72
 Millholland, S., Wang, S., & Laughlin, G. 2017, *ApJ*, 849, L33
 Mills, S. M., Howard, A. W., Weiss, L. M., et al. 2019, *AJ*, 157, 145
 Murray, C. D., & Dermott, S. F. 2010, *Solar System Dynamics* (Cambridge: Cambridge Univ. Press)
 Nissen, P. E., Christensen-Dalsgaard, J., Mosumgaard, J. R., et al. 2020, *A&A*, 640, A81
 Ofir, A., Dreizler, S., Zechmeister, M., & Husser, T.-O. 2014, *A&A*, 561, A103
 Owen, J. E., & Wu, Y. 2017, *ApJ*, 847, 29
 Parviainen, H., & Aigrain, S. 2015, *MNRAS*, 453, 3821
 Pecalet, M. J., & Mamajek, E. E. 2013, *ApJS*, 208, 9
 Petigura, E. A., Howard, A. W., Marcy, G. W., et al. 2017, *AJ*, 154, 107
 Petigura, E. A., Marcy, G. W., & Howard, A. W. 2013, *ApJ*, 770, 69
 Piaulet, C., Benneke, B., Rubenzahl, R. A., et al. 2021, *AJ*, 161, 70
 Pollack, J. B., Hubickyj, O., Bodenheimer, P., et al. 1996, *Icar*, 124, 62
 Rice, M., & Brewer, J. M. 2020, *ApJ*, 898, 119

- Ricker, G. R., Winn, J. N., Vanderspek, R., et al. 2015, *JATIS*, **1**, 014003
- Rogers, L. A. 2015, *ApJ*, **801**, 41
- Rossiter, R. A. 1924, *ApJ*, **60**, 15
- Rubenzahl, R. A., Dai, F., Howard, A. W., et al. 2021, *AJ*, **161**, 119
- Salvatier, J., Wiecki, T. V., & Fonnesbeck, C. 2016, *PeerJ Comp. Sci.*, **2**, e55
- Scarsdale, N., Murphy, J. M. A., Batalha, N. M., et al. 2021, *AJ*, **162**, 215
- Schlaufman, K. C. 2018, *ApJ*, **853**, 37
- Stassun, K. G., Oelkers, R. J., Pepper, J., et al. 2018, *AJ*, **156**, 102
- Tayar, J., Claytor, Z. R., Huber, D., & van Saders, J. 2020, arXiv:2012.07957
- Theano Development Team 2016, arXiv:1605.02688
- Valenti, J. A., Butler, R. P., & Marcy, G. W. 1995, *PASP*, **107**, 966
- Van Der Walt, S., Colbert, S. C., & Varoquaux, G. 2011, arXiv:1102.1523
- Van Eylen, V., Agentoft, C., Lundkvist, M. S., et al. 2018, *MNRAS*, **479**, 4786
- Vogt, S. S., Radovan, M., Kibrick, R., et al. 2014, *PASP*, **126**, 359
- Wakeford, H. R., Wilson, T. J., Stevenson, K. B., & Lewis, N. K. 2019, *RNAAS*, **3**, 7
- Weiss, L. M., Dai, F., Huber, D., et al. 2021, *AJ*, **161**, 56
- Weiss, L. M., & Marcy, G. W. 2014, *ApJL*, **783**, L6
- Weiss, L. M., Marcy, G. W., Petigura, E. A., et al. 2018, *AJ*, **155**, 48
- Zechmeister, M., & Kürster, M. 2009, *A&A*, **496**, 577
- Zeng, L., Sasselov, D. D., & Jacobsen, S. B. 2016, *ApJ*, **819**, 127
- Zhang, J., Weiss, L. M., Huber, D., et al. 2021, *AJ*, **162**, 89
- Zhu, W., & Wu, Y. 2018, *AJ*, **156**, 92